Theor. Comput. Fluid Dyn. (2018) 32:753–764
https://doi.org/10.1007/s00162-018-0475-z

ORIGINAL ARTICLE

Xiaolong Zhang · Mohammad Abul Hashem · Xiaolin Chen · Hua Tan

On passing a non-Newtonian circulating tumor cell (CTC) through a deformation-based microfluidic chip

Received: 12 March 2018 / Accepted: 18 August 2018 / Published online: 29 August 2018

Abstract Circulating tumor cells (CTCs) are potential indicators of cancer. Detection of CTCs is important for diagnosing cancer at an early stage and predicting the effectiveness of cancer treatment. Among various devices, deformation-based CTC microchips have shown a strong promise for CTC detection. This type of devices involves a process where CTCs are trapped while allowing more deformable blood cells to squeeze through the filtration geometry at the specified operating pressure. For designing a reliable CTC microchip, in-depth understanding of the cell passing process through the deformation-based microfluidic device is of high value to the device performance enhancement. In this paper, the CTC squeezing process through a microfluidic filtering channel is studied with a non-Newtonian CTC model employed to account for shear-thinning properties of the cell. Detailed microscopic multiphase flow characteristics regarding the filtering process are discussed including the pressure signatures, flow details, cell deformation, and viscosity variation. Critical pressure for the non-Newtonian CTC at different flow rates is analyzed as it plays a crucial role in the device operation in ensuring a successful passing event. Our study provides insights into the non-Newtonian cell squeezing process, which can guide in the design and optimization of next-generation deformation-based CTC microfilters.

Keywords CTC · Non-Newtonian model · Deformation-based microfluidic chip · Critical passing pressure

1 Introduction

Cancer is a large family of diseases which forms a subset of neoplasms or tumors, a group of cells that have undergone an abnormal growth. It has the potential to spread from the originating organ to another organ through the cardiovascular system by a process called metastasis, which is identified as the main factor of death due to cancer. Most of the cancer patients do not die of the direct effects of the primary tumor, rather die of metastatic diseases [1]. The presence of CTCs in the peripheral blood of cancer patients is found to be a potential biomarker of early tumor formation [2]. Extreme rarity and heterogeneity cause CTC detection very challenging. The frequency of CTCs is on the order of 1–3000 CTCs per ml of blood of a metastasis disease patient [3], where there are 10^7 white blood cells (WBCs) and 10^9 red blood cells (RBCs) in the same amount of blood [4]. Any CTC detection technique is required to be able to separate this small number of cells from blood. Also, CTCs share some properties in common with the leukocytes (WBCs) and hence contributing to making the discrimination technique more difficult. CTCs can be discriminated using their unique biological and physical properties from highly abundant RBCs and WBCs. Biological properties are,

Communicated by Tim Phillips.

X. Zhang · M. A. Hashem · X. Chen (✉) · H. Tan
Mechanical Engineering, School of Engineering and Computer Science, Washington State University Vancouver, Vancouver, WA 98686, USA
E-mail: chenx@wsu.edu

for example, expression of surface protein not expressed in other blood cells, the presence of specific genes, viability, etc. Physical properties include the size of CTC, shape, density, deformability, dielectric properties, magnetic susceptibility, etc.

Depending on their properties, current CTC separation techniques are categorized as biochemical methods and biophysical methods. Biochemical CTC separation methods separate CTCs by using antigen-antibody binding properties. Techniques employed by these methods include magnetic nanoparticle-based separation (immunomagnetic assay) [3], microfluidic separation [5], and the combination of microfluidic separation and immunomagnetic assay [6]. In the current biochemical approaches, there is a chance of losing expression for the epithelial marker (such as EpCAM and CK) because a subpopulation of metastatic tumor cells tends to undergo epithelial to mesenchymal transition [7]. On the other hand, physical CTC separation methods are filter-based which usually employ the physical properties of CTCs, and provide the advantage of avoiding epithelial antigen bias associated with biochemical methods. A potential biomarker of CTCs is their greater size relative to other blood cells, which inspired the emerge of size-based CTC separation techniques like hydrodynamic chromatography [8], dielectrophoresis [9], acoustophoresis [10], inertial flow [11], deterministic lateral displacement (DLD) [12,13], and filtration of fixed cell samples [14]. However, some studies found that there is a significant overlap of size between leukocytes and CTCs derived from some specific tumors, which may reduce the effectiveness of size-based separation methods [15].

In a study of breast cancer patients, Meng et al. reported that the average nuclear to cytoplasmic ratio (N/C) of CTCs was 4.0 and leukocytes was 1.22 which causes cancer cells to be less deformable than blood cells [16]. Therefore, significantly stiffer CTCs can be discriminated potentially from the blood cells based on deformability despite their identical size. There are different types of deformation-based filtration microstructure for the separation of CTCs. Weir, pillar, pore, and microscale confinement channels are most common. McFaul et al. introduced a microfluidic structural ratchet mechanism based on size and deformability to separate the cells [17]. The separation is highly selective, and their device uses oscillatory flow to improve the unclogging in the microfilters. Tan et al. proposed a device employing size and deformability properties where multiple arrays of crescent-shaped isolation wells are created to trap the cancer cells [18]. Along with the experimental studies, numerical simulation emerges as a powerful tool to predict the behavior of a cell inside a microfilter and may deliver important insights to optimize the processes by saving time and cost. Aghaamoo et al. used numerical simulation to analyze the pressure-deformability behavior of the cancer cell when filtered by a conical shaped microfilter [19]. Based on their analysis, they identified the critical pressure and deformations in the forward and backward direction.

The key feature for numerical simulation of deformation-based microfiltration is mechanical modeling of the cell. For modeling the living cells, there are mainly two approaches: micro/nanostructural approach [20] and continuum approach [21]. The former approach focuses on the cell behaviors and response on the subcellular level, where the latter approach considers the cell consists of continuum materials. The continuum model is advantageous when modeling the complex interactions between the cell, channel, and blood plasma during the filtration process. This model is classified into liquid droplet model and solid model. For the large deformation problems, liquid droplet model can predict better than the solid model [22]. This model assumes that the cell consists of a homogeneous liquid encapsulated by a cortical membrane. The cortical membrane is an anisotropic viscous fluid layer with constant surface tension.

According to the existing research, CTCs exhibit a highly variable viscosity with a large variation ranges from 0.001 Pa.s to above 1000 Pa.s, which brings a big challenge for cell modeling [22,23]. The behavior of a cell is dominated by the cytoplasm as it occupies almost 78% of the cell volume [24]. Though cytoplasm mostly contains water, there are highly concentrated proteins, granules, filamentous components, mitochondria, etc., and the presence of these elements significantly influences the cell behavior to be non-Newtonian [25,26]. Many living cells including tumor cells are characterized by a shear-thinning property, which is demonstrated by a varying cell viscosity dependent on the cell deformation [27]. Tsai et al. developed model to analyze the non-Newtonian behavior of passive human neutrophils [28]. Their study demonstrates that apparent viscosity of neutrophil cytoplasm depends on aspiration pressure and mean shear rate. This dependency of cytoplasmic viscosity on mean shear rate is expressed as a power-law relationship. In this paper, a non-Newtonian cell model is built up to consider the effects of non-Newtonian properties on the passing process of the CTC through the microfluidic channel. The motion, deformation, and pressure signatures of the non-Newtonian CTC passing through the microfilter are studied and discussed in detail. Also discussed are the effects of flow rate on the cell behavior and microfiltration process. Theoretical methods and empirical formulae are proposed for the quick estimation of the system pressure, which drives the microfiltration process and significantly determines the

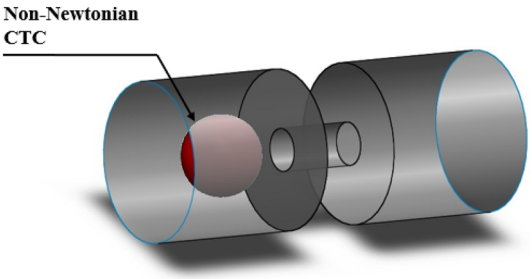

Fig. 1 Non-Newtonian cell model and microfilter configuration

performance of the device. With the non-Newtonian effects taken into consideration, the theoretical methods and formulae can be applied to the design and optimization of deformation-based CTC chips for better accuracy.

2 Methodology

2.1 Operation principle

In the deformation-based microfilter, the CTC is pushed through the filtration channel by the operating pressure imposed on the inlet of the microfilter. This operating pressure on the inlet is defined as the system pressure, and its variation with respect to time is termed as the pressure profile which conveys important signatures of the CTC passing process. The system pressure is used to overcome the resistance in the microfilter, and it is maximum when the CTC starts to squeeze into the filtration channel [29]. The maximum system pressure is typically referred to as the critical pressure, which is a significant factor to ensure a successful cell passing process. When the system pressure of the device is kept below the critical pressure of CTCs and above the critical pressure of normal blood cells, the CTCs are trapped in the chamber while other pliable normal blood cells can get through. In this study, we modeled CTC as a simple liquid droplet of non-Newtonian fluid. Multiphase flow employs a single CTC and blood plasma as the carrier fluid. Illustrated in Fig. 1 is the physical model of a CTC squeezing through the deformation-based microfilter.

The microfilter consists of the entrance chamber, exit chamber, and filtration channel. The entrance and exit chambers are identical cylinders with a radius (r_{cham}) of 15 μm and a length of 30 μm. The cylindrical filtration channel adopted here is 15 μm long with a radius of (r_{ch}) of 4 μm. CTC is considered to be 16 μm in diameter, and surface tension coefficient is 0.05 N/m [30].

The system pressure is often decomposed into two parts to overcome two types of resistance in the microfilter. The decomposition can be expressed as

$$P_{\text{system}} = P_{\text{surface}} + P_{\text{viscous}} \tag{1}$$

in which the former part P_{surface} is the pressure to overcome the surface tension and the latter part P_{viscous} is the pressure to overcome the viscous resistance in the microfilter. The surface tension-induced pressure P_{surface} can be evaluated by using the following Young–Laplace equation. Particularly, if the flow rate in the microfilter is very low, the initial stage of the cell squeezing into the filtration channel can be approximated by a quasi-static aspiration process. In the quasi-static case, we can assume that the aspirated part and non-aspirated part of the cell are spherical, so the surface tension-induced pressure P_{surface} has the expression

$$P_{\text{surface}} = 2\sigma \left(\frac{1}{r_{\text{ch}}} - \frac{1}{r_{\text{cell}}} \right) \tag{2}$$

where σ is the surface tension, r_{ch} and r_{cell} are the radii of aspirated and non-aspirated part of the interface curvature during squeezing-in.

The viscous pressure P_{viscous} is expressed as

$$P_{\text{viscous}} = \frac{8\mu L V}{r_{\text{ch}}^2} + K_c \frac{\rho V^2}{2} + K_e \frac{\rho V^2}{2} \tag{3}$$

where ρ and μ are the density and viscosity of blood plasma respectively, L is the length of filtration channel, V is the local flow velocity, and K_c and K_e are the pressure loss coefficients. K_c and K_e are set as 0.5 and 1, respectively, assuming the filtering channel is much smaller than the filtering chambers.

2.2 Mathematical model

The flow in the microfilter is governed by the continuity and momentum equations which are expressed as,

$$\begin{cases} \frac{\partial}{\partial t}(\rho) + \nabla \cdot (\rho \vec{u}) = 0 \\ \frac{\partial}{\partial t}(\rho \vec{u}) + \nabla \cdot (\rho \vec{u}\vec{u}) = -\nabla p + \nabla \cdot (\mu(\nabla \vec{u} + \nabla \vec{u}^T)) + \rho \vec{g} + \vec{F} \end{cases}, \tag{4}$$

where ρ is fluid density, u is the flow velocity, p is the pressure, $\vec{g}$ is gravitational acceleration vector, $\vec{F}$ represents the source term such as the interfacial forces, and μ is the dynamic viscosity. Since the viscous cancer cell and the blood plasma establish a two-phase flow, so the dynamic viscosity μ in the governing equation (Eq. 4) varies according to different phases. In the current study, the blood plasma is assumed to be Newtonian fluid with a constant viscosity $\mu_f = 0.001$ Pa · s. The CTC is modeled by a non-Newtonian simple liquid droplet model with shear-thinning fluid encapsulated by constant surface tension (cell membrane), as shown in Fig. 1. The viscosity of the non-Newtonian cell is dependent on the varying cell deformation during the passing process. In other words, the cell viscosity is dependent on the strain rate and can be expressed as $\mu = \mu(\boldsymbol{S})$, in which $\boldsymbol{S}$ is the strain tensor

$$\boldsymbol{S} = \left(\frac{\partial u_j}{\partial x_i} + \frac{\partial u_i}{\partial x_j} \right) \tag{5}$$

For simplification, the cell viscosity can be assumed to be determined by the second invariant of the stain tensor $\boldsymbol{S}$, which is defined as

$$\dot{\gamma} = \sqrt{\frac{1}{2}\boldsymbol{S} : \boldsymbol{S}}; \tag{6}$$

hence, the cell viscosity is expressed as $\mu = \mu(\dot{\gamma})$. For cell viscosity independent of temperature, the viscosity can be modeled by the power-law expression

$$\mu = k\dot{\gamma}^{n-1} \tag{7}$$

where k is the consistency index which represents an average viscosity of the cell fluid, and n is the power-law index which represents the deviation from the Newtonian fluid. When $n = 1$, it means Newtonian fluid; When $n > 1$, it is dilatant fluid with shear-thickening properties; and when $n < 1$, it is termed as pseudo-plastic fluid with shear-thinning properties. For the current study, the CTC is modeled as shear-thinning fluid with the power-law index of 0.48, as indicated by existing research [28]. Consistency index is set to $k = 1.00$ kg-s^{n-2}/m. After the viscosity modeling, the local shear stress $\boldsymbol{\tau}$, which closely relates to the pressure drop in the microfilter, is then calculated based on the stress–strain relation $\boldsymbol{\tau} = \mu \cdot \boldsymbol{S}$. The internal cell structure (such as the DNA sequence, lipid layer, and cytoskeleton) and the internal flow details (such as vortex inside the cell) are not considered for convenience.

The phases in the microfilter are treated as immiscible fluids, and the cell membrane is represented by the interface between the two phases. The interface can be tracked by solving the continuity equation of different phases. For the kth fluid, the equation is given by

$$\frac{\partial}{\partial t}(\alpha_k \rho_k) + \nabla \cdot (\alpha_k \rho_k \vec{u}_k) = S_k + \sum_{l=1}^{n} (\dot{m}_{lk} - \dot{m}_{kl}) \tag{8}$$

where ρ_k denotes the density of the kth fluid; $\vec{u}_k$ denotes the velocity; S_k denotes the mass source term which is zero in this problem; $\dot{m}_{lk}$ denotes the mass transfer from the lth to the kth fluid, and $\dot{m}_{kl}$ denotes the mass transfer from the kth to the lth fluid. In this study, we assume there is no mass transfer between different phases.

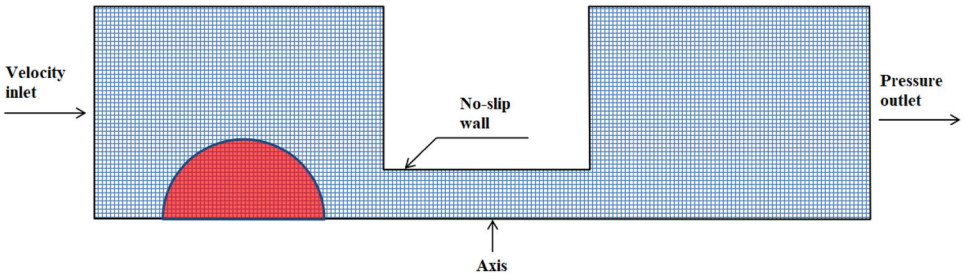

Fig. 2 2D axisymmetric mesh structure of the computation domain

2.3 Simulation method

Various methods are available for interface tracking, including level-set, front tracking, and volume of fluid (VOF) methods. In this paper, the VOF model is employed as it conserves mass well without having logic problems related to intersecting surfaces. Geometric reconstruction scheme is selected for performing interpolation near the interface. The surface tension of the cell membrane is modeled by the continuum surface force (CSF) method, to evaluate the surface tension effects accurately without imposing restrictions on modeling the dynamic evolution of the cell-blood interface. To save computational cost in solving the governing equations, a 2-D axisymmetric analysis is employed in this study. The grid convergence study has been carried out to show that grid size is small enough to generate grid independent results. The mesh of the computation domain consists of 384,000 uniform quadratic Cartesian grid cells, where 42,000 grid cells are patched for the CTC (Fig. 2). The discretization of governing equations is done by the second-order implicit differentiating scheme. Velocity inlet boundary condition is set at the entrance of the filtration channel, and pressure outlet condition is applied at the exit. The flow rates for different cases vary from 14 to 63 nl/s, which falls within the commonly reported operating range [31]. No-slip, non-wetting boundary conditions are prescribed on the channel walls with a contact angle of 180°.

3 Results and discussion

3.1 Pressure signatures

The system pressure plays a key role in the CTC passing process as cell filtration is driven by the operating pressure of the deformation-based filtration system. The pressure signatures (i.e., the pressure profile and the critical pressure) of the filtration process provide very useful guidance for the device design and optimization. The pressure profiles at different flow rates ($Q = 14$ nl/s $\sim$ 63 nl/s) are studied in this section for a comprehensive investigation. Figure 3 presents a few representative pressure profiles at different flow rates with the deformed cell at various stages of the passing process.

Although these passing processes at different flow rates share the same trend characterized by similar stages (e.g., cell squeezing-in, cell occupation in filtration channel, and cell squeezing-out) with similar cell deformations, one can see the pressure signature notably affected by the flow rate variation. During the cell progression through the inlet chamber (stage I), the system pressure remains almost constant until the cell reaches the entrance of the microfiltration channel. The horizontal segments of the pressure profiles represent viscous pressure as surface tension-induced pressure is negligible at this stage. Cell deformation in stage I is very little compared to other stages. At the entrance of the filtration channel, the cell goes through a significant deformation (stage II). System pressure suddenly jumps to a higher value as to push the stiffer cell through the narrower channel. The peaks of the pressure profiles represent critical pressure (P_{critical}), which is the pressure required to overcome the resistance at the entrance of the microfiltration channel. For very low flow rates ($Q \leq 21$ nl/s), the pressure is maintained at a high level when leading edge of the cell changes from spherical to a cylindrical shape (stage II) in contrast to falling sharply like higher flow rate cases.

During the cell occupation stage (stage II–VI), when the cell fully occupies the filtration channel, the radius of curvature of trailing edge decreases gradually. As a result, there is a gradual decrease in surface tension-induced pressure according to the Young–Laplace equation. At stage IV, the radius of curvature of both ends is equal, and net surface tension-induced pressure becomes zero. Thus, the system pressure as shown in the

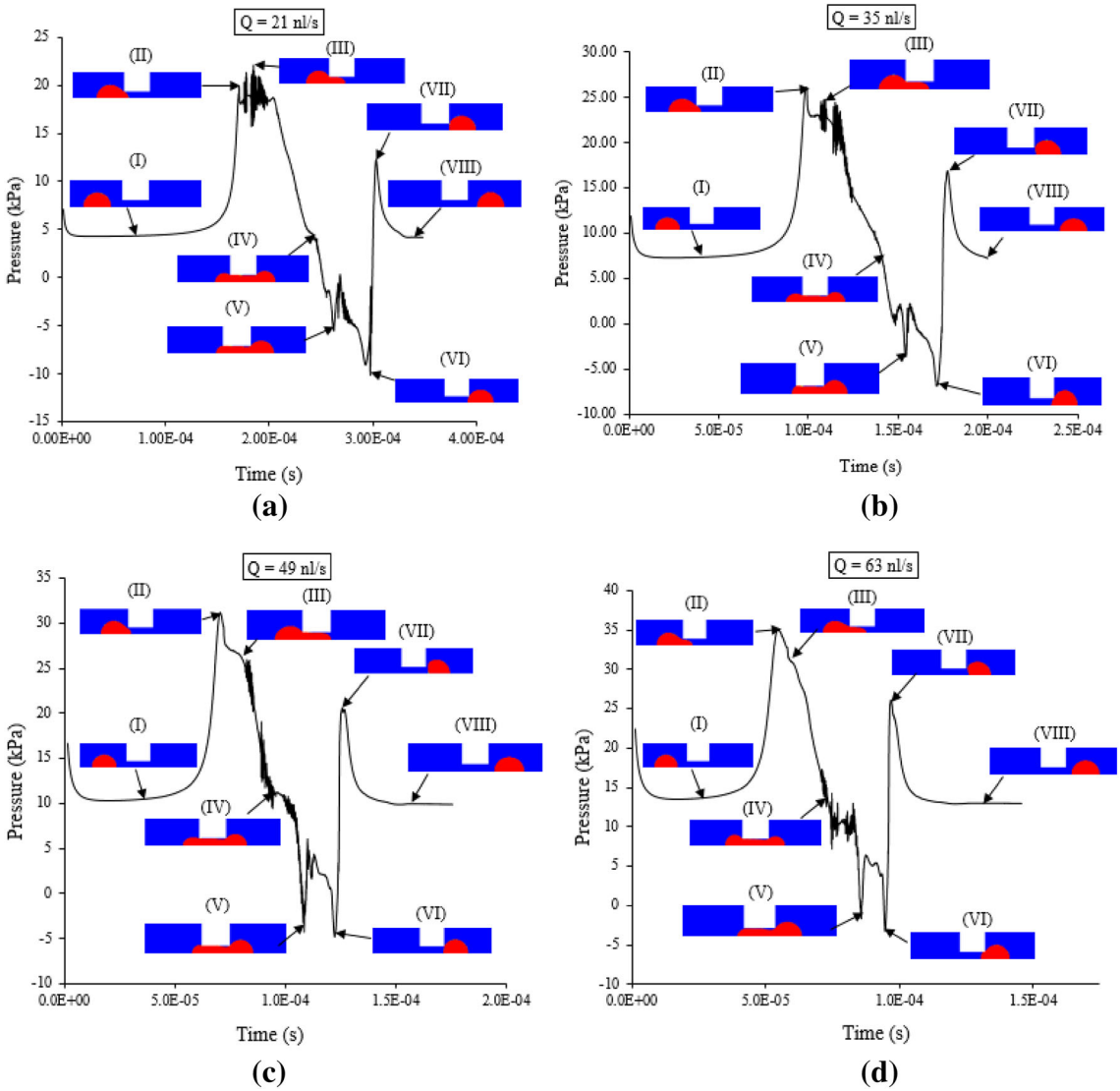

Fig. 3 Pressure signatures with cell deformation during the pass-through process: **a** $Q = 21$ nl/s, **b** $Q = 35$ nl/s, **c** $Q = 49$ nl/s and **d** $Q = 63$ nl/s

figure reaches the same level of viscous pressure. After this stage, the resultant force due to surface tension changes the direction and acts to pull out the cell from the filtration channel, which causes the reduction in the system pressure. Minimum pressure occurs at stage VI when the cell is about to squeeze out, and cell deformation is just opposite to the case of cell squeezing-in. When the cell entirely leaves the filtration channel (stage VII), another peak pressure is observed which is less than the value of critical pressure. This maximum local pressure arises due to the bouncing of the rear part of the cell for inertia effects. In the exit chamber (stage VIII), the system pressure reaches a constant value equal to that of the inlet chamber as deformed cell recovers the original spherical shape.

For comparison, we studied the behavior of Newtonian Cell model for different viscosities with flow rate $Q = 35$ nl/s. Figure 4 represents the pressure signatures for a Newtonian cell model with CTC viscosity 0.012 Pa.s and a non-Newtonian cell model with varying viscosity. Note that viscous pressure drop is identical for both model types because there is no significant impact of shear stress on the cell during passing through the inlet and exit chambers. Newtonian cell maintains a high level of pressure after leading edge enters into the filtration channel and block the entrance, which is similar to the low flow rate cases of the non-Newtonian model. From the magnified image of the microfiltration channel, it is clear that highly viscous Newtonian cell has more adhesion with the channel wall during occupation stage, which causes this higher pressure. In contrast

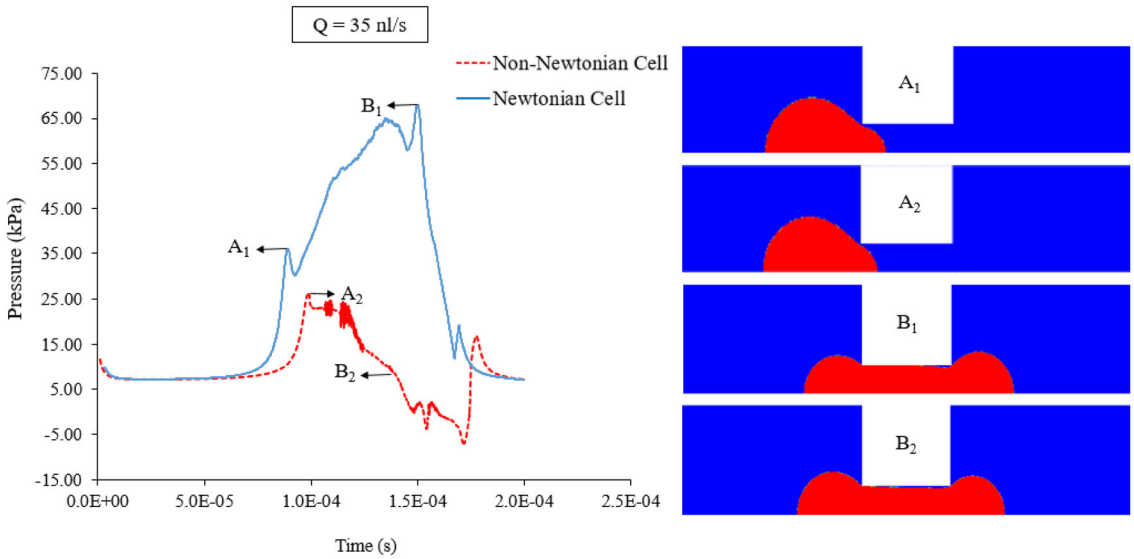

Fig. 4 Pressure signatures of Newtonian and non-Newtonian cell model: A_1 and A_2 represent the cell squeezing-in stages, B_1 and B_2 represent the cell occupation stages

to the non-Newtonian model, peak pressure does not necessarily occur during the Newtonian cell entering into the filtration channel. In case of lower flow rates, the Newtonian cell requires higher pressure during initial aspiration. However, for higher flow rates and highly viscous cell, the channel is blocked more during cell occupation stage due to the increased adhesive force between the wall and cell surface. As a result, peak pressure occurs during the cell occupation stage. For convenience, we studied Newtonian cells with viscosity 0.004 Pa.s, 0.008 Pa.s and 0.012 Pa.s. and observed similar phenomena. Our study shows a good agreement with the previous work [32].

3.2 Effects of flow rates on pressure

Since the critical pressure plays a significant role in ensuring a successful CTC passing event, the critical pressure of all the simulated cases is plotted in Fig. 5 for an in-depth analysis and characterization. Also given in the figure are the decomposed components of the critical pressure with respect to flow rate. Based on simulation results, empirical formulae are proposed for the viscous pressure and surface tension-induced pressure, which is discussed in the later sections. One can see a linear growth of the critical pressure and viscous pressure with the increment of flow rate. For the spherical assumption of aspirated and non-aspirated parts of the cell, the predicted surface tension-induced pressure from Eq. (2) is 12.5 kPa. In reality, the cell experiences uneven deformation during squeezing through the filtration channel. Non-spherical deformed parts cause higher surface tension-induced pressure than the predicted value. Observed surface tension-induced pressure increases linearly with increasing the flow rate though the change is little in compared to the change in critical and viscous pressure.

Since the system pressure consists of the viscous pressure drop P_{viscous} and the surface tension-induced pressure drop P_{surface}, two parts are analyzed separately for convenience. As is known, the viscous pressure drop for channel flow P_{viscous} is determined by Eq. (3). For the current case, there exist interactions between the cell and the ambient blood plasma during the passing process. So the effects of the non-Newtonian cell on the viscous pressure drop should be taken into consideration. Since the non-Newtonian cell has changing shear stress dependent on the varying cell deformation and movement during the passing process, it seems impossible to analytically estimate the effects from the cell. Hereby, a simple correction coefficient ε is introduced to account for the effects from the non-Newtonian cell. It is assumed that the non-Newtonian cell affects the viscous pressure in an invariant way regardless of the flow rate variation. In other words, the effects from the non-Newtonian cell on the viscous pressure are assumed to be simply proportional to the corresponding viscous pressure by a constant coefficient ε, which is a non-dimensional number independent of velocity. Based on the assumption above, the viscous pressure is expressed as

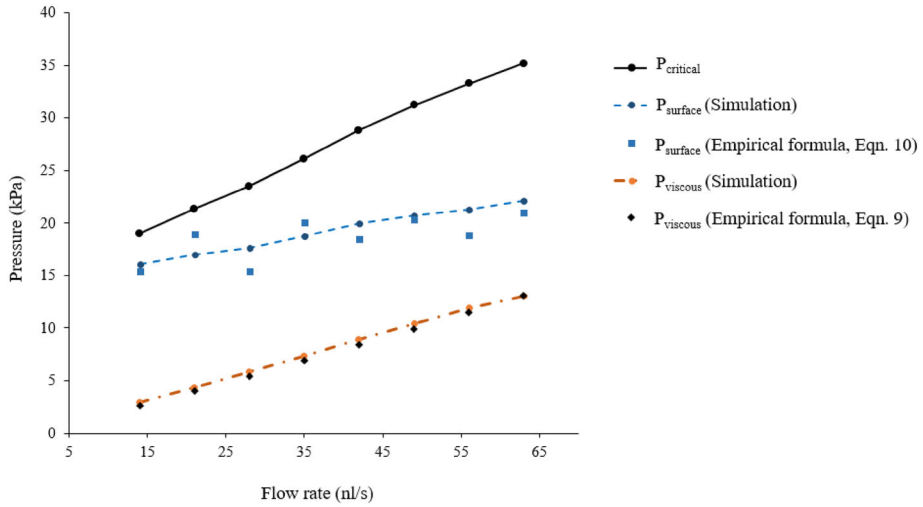

Fig. 5 Critical pressure and its components with respect to different flow rates

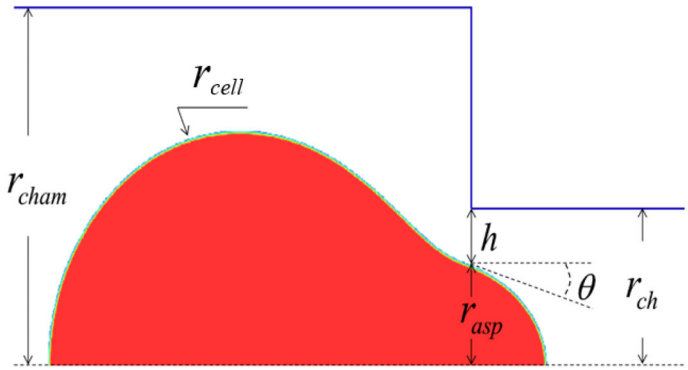

Fig. 6 Schematic view of deformed cell squeezing into the filtration channel

$$P_{\text{viscous}} = (1+\varepsilon)\left(\frac{8\mu LV}{r_{\text{ch}}^2} + K_c\frac{\rho V^2}{2} + K_e\frac{\rho V^2}{2}\right) \tag{9}$$

where ε is the constant coefficient which can be obtained based on the simulation data. The value of ε is dependent on device design and can be determined from the linear fit of the simulation data. By applying the least square method to the simulation data, one can get the value $\varepsilon = 0.22$. One can see the predicted result from Eq. (9), which is also presented in Fig. 5 and agrees well with simulation data.

As stated earlier, the spherical assumption is not completely valid for the deformed non-Newtonian cell, in which the increased shear stress will lead to an enhanced and notable cell stretching in the longitudinal direction. As shown in Fig. 6, the enhanced longitudinal stretching finally results in a non-spherical aspirated tip with larger curvature during the stage of squeezing-in, in which the maximum value of the system pressure also occurs according to the Young–Laplace theorem. The surface tension-induced pressure can be estimated based on the general form of Young–Laplace relation (Eq. 2) and the force balance on the cell. After modification, surface tension-induced pressure is finally obtained with the following expression

$$P_{\text{surface}} = 2\sigma\left(\frac{1}{r_{\text{asp}}\cos(\theta)} - \frac{1}{r_{\text{cell}}}\right), \tag{10}$$

where σ is the surface tension of the cell, r_{cell} is the cell radius which is assumed to be constant for simplicity, h is the gap between the non-Newtonian cell and the wall at the filtration channel entrance, $r_{\text{asp}} = r_{\text{ch}} - h$ is the cross section radius of the aspirated part at the entrance, and θ is the local angle of cell membrane at the filtration channel entrance. The surface tension-induced pressure obtained from the simulation and from the modified Young–Laplace equation is close enough as shown in Fig. 5.

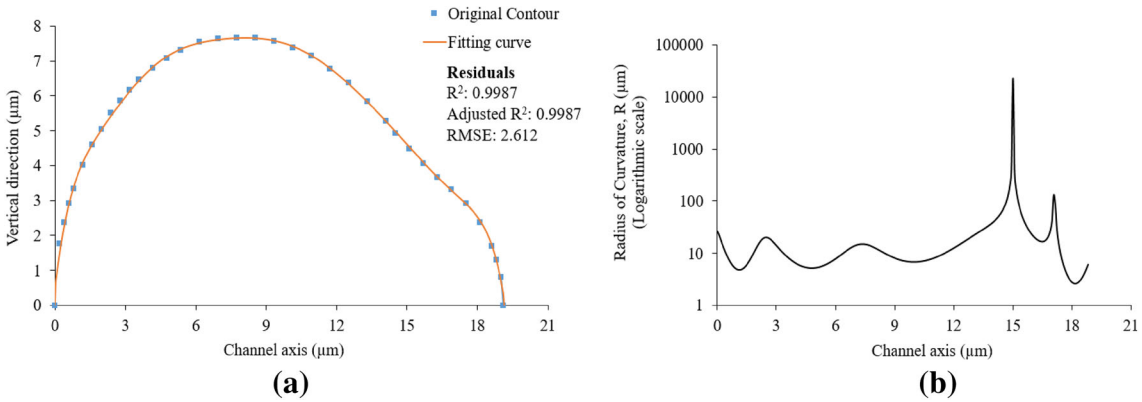

Fig. 7 Radius of curvature of the deformed CTC during entering into the filtration channel for flow rate $Q = 35$ nl/s: **a** Original contour and fitted curve and **b** variation of radius of curvature along the cell interface

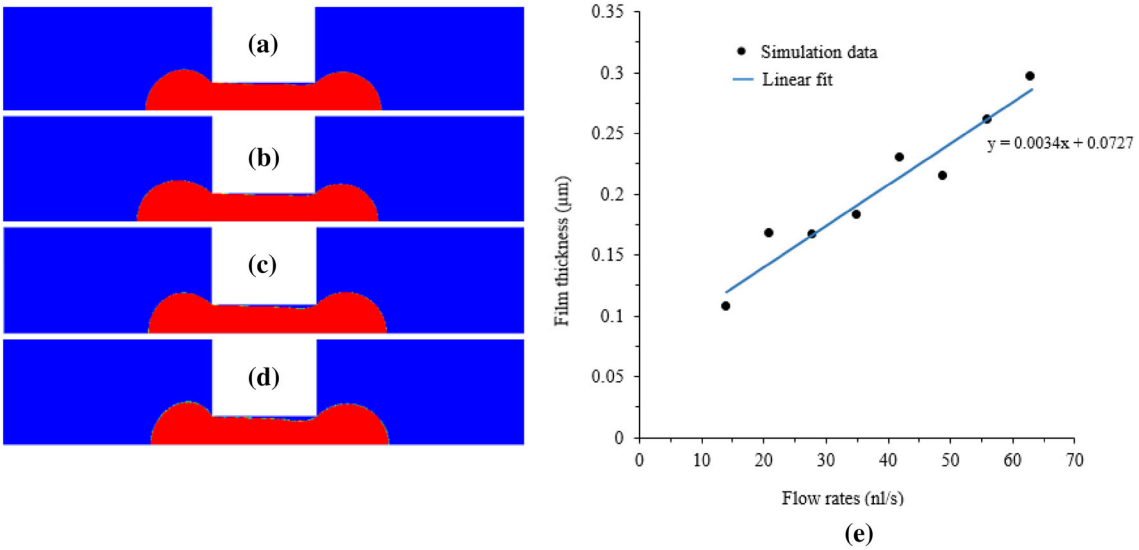

Fig. 8 Film gap evolution during the cell pass-through process: **a** $Q = 21$ nl/s, **b** $Q = 35$ nl/s, **c** $Q = 49$ nl/s, **d** $Q = 63$ nl/s, **e** variation of average film thickness with flow rate

To demonstrate deformations analytically, we calculated the radius of curvature of the cell at various locations of the interface for a typical flow rate case ($Q = 35$ nl/s). Cell interface was traced using MATLAB. Origin was set at the intersection of cell interface and the centerline of the microchannel, and the smooth fitting curve was found using 10th order polynomial equation. We calculated the local radii of curvature at cell interface by adopting finite difference method, and the variation is depicted in Fig. 7. It is clear from Fig. 7b that radius of curvature is not uniform along the cell interface. This deviation from spherical shape is the key factor for higher surface tension-induced pressure than the predicted value (12.5 kPa) by Young–Laplace equation. It is to be mentioned that the instantaneous peak values of radius of curvature at some locations of the interface are due to the elongated straight regions of the interface.

3.3 Cell deformation

Given in Fig. 8a–d are parts of the cell deformations when the cell fully occupies the filtration channel at different flow rates. Interestingly, one can see a thin film gap between the non-Newtonian cell and the channel wall, which is very similar to the previous research with Newtonian cell model [31–33]. The average thickness of thin film gap between the non-Newtonian cell and channel wall is given in Fig. 8e.

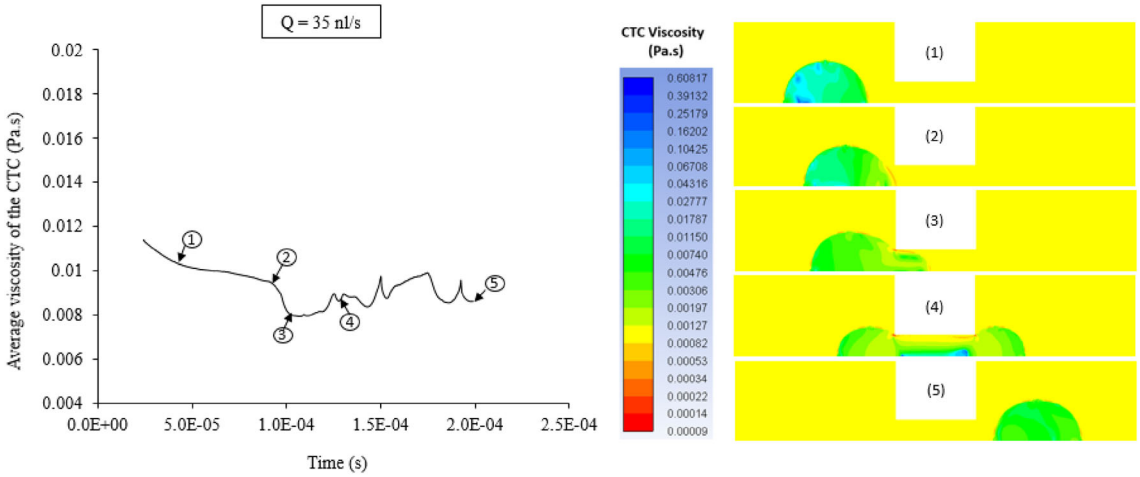

Fig. 9 Viscosity variation during the CTC squeezing process: **a** viscosity profile by taking cell average viscosity and **b** viscosity distribution of flow domain at different stages

One can see a linear increase in the averaged thin film thickness as the flow rate increases. For the interest of quantitatively characterizing the thin film thickness, theories have been proposed based on scaling analysis of the two-phase flow in channels with elongated drops [34]. Unfortunately, these theories are based on the assumptions of Newtonian fluids and drops in the channel. For this current research, the non-Newtonian cell has varying viscosity dependent on the transient cell deformation, which makes the quantitative characterization of the thin film thickness more challenging. This paper does not elaborate much on this point since the cell occupation stage maintains a low system pressure compared to the critical pressure, which means limited effects on the CTC passing process. However, considering the promising applications of non-Newtonian flows in various fields, corresponding research is also highly desired.

The pressure-driven two-phase flow of blood plasma and CTC experiences shear stress which varies with the contraction and expansion of the channel. Non-Newtonian CTC exhibits shear-thinning property during squeezing through the microchannel. The viscosity variation of CTC is illustrated in Fig. 9 along with the deformed cell at various stages of filtration for a representative flow rate $Q = 35$ nl/s. It is clear from the illustration that viscosity distribution within the deformed cell is not uniform due to the effect of wall shear stress. At the cell occupation stage (Fig. 9b-(4)), one can notice that viscosity is higher in the axis region, gradually decreases in the vertical direction and is minimum near the channel wall where shear rate is the highest. We observed the cell average viscosity during squeezing process, and viscosity profile is depicted in Fig. 9a. It is clear that cell viscosity is considerably affected by the shear stress at different stages of squeezing process. When the cell fully occupies the filtration channel, the value is minimum as the shear rate is higher in this region. The oscillations at the occupation stage are due to the presence of non-uniform thin film gap which reduces the impact of shear stress on the cell surface. With the decrease of shear rate in the exit chamber, viscosity rises to the previous level as that of inlet chamber though there are still some oscillations in the curve. The reason is after going through deformation; it takes a reasonable time to recover the original spherical shape which is not achieved in our limited time steps.

4 Conclusions

In this study, pressure signatures for different flow rates are characterized numerically. We found that critical pressure increases with the increase in the flow rate. Pressure signatures for Newtonian and non-Newtonian cell model are compared for in-depth understanding. It is noticeable that critical pressure for higher flow rate cases ($Q \geq 21$ nl/s) of the non-Newtonian model occurs when the cell starts squeezing in. On the other hand, for Newtonian cell model and lower flow rate cases of the non-Newtonian model, system pressure gradually rises to a higher level after the beginning of squeezing-in process. Critical pressure occurs when the cell fully blocks the entrance of the filtration channel. Due to the non-spherical cell deformation, surface tension-induced pressure and viscous pressure slightly deviate from their predicted values. Based on numerical results,

modified formulae have been proposed for viscous pressure and surface tension-induced pressure. During cell occupation stage, a thin film filled with career fluid forms and the film thickness changes linearly with the flow rate. Non-Newtonian cell exhibits shear-thinning property, i.e., variable viscosity with the change of shear rate during filtration process. Our study provides insights into the dynamics of a non-Newtonian cell passing through the constricted microchannel. Details of flow physics and proposed empirical formulae can play an important role for quick evaluation, design, and optimization of such deformation-based CTC microfluidic chips.

References

1. Dong, Y., Skelley, A., Merdek, K., Sprott, K., Jiang, C., Pierceall, W., Lin, J., Stocum, M., Carney, W., Smirnov, D.: Microfluidics and circulating tumor cells. JMD **15**(2), 149–157 (2013)
2. Fabbri, F., Carloni, S., Zoli, W., Ulivi, P., Gallerani, G., Fici, P., Chiadini, E., Passardi, A., Frassineti, G.L., Ragazzini, A.: Detection and recovery of circulating colon cancer cells using a dielectrophoresis-based device: KRAS mutation status in pure CTCs. Cancer Lett. **335**(1), 225–231 (2013)
3. Allard, W.J., Matera, J., Miller, M.C., Repollet, M., Connelly, M.C., Rao, C., Tibbe, A.G., Uhr, J.W., Terstappen, L.W.: Tumor cells circulate in the peripheral blood of all major carcinomas but not in healthy subjects or patients with nonmalignant diseases. Clin. Cancer Res. **10**(20), 6897–6904 (2004)
4. Young, B., Lowe, J., Stevens, A., Heath, J.: Wheater's Functional Histology: A Text and Colour Atlas Churchill Livingstone. Elsevier, New York (2006)
5. Nagrath, S., Sequist, L.V., Maheswaran, S., Bell, D.W., Irimia, D., Ulkus, L., Smith, M.R., Kwak, E.L., Digumarthy, S., Muzikansky, A.: Isolation of rare circulating tumour cells in cancer patients by microchip technology. Nature **450**(7173), 1235 (2007)
6. Hoshino, K., Huang, Y.-Y., Lane, N., Huebschman, M., Uhr, J.W., Frenkel, E.P., Zhang, X.: Microchip-based immunomagnetic detection of circulating tumor cells. Lab Chip **11**(20), 3449–3457 (2011)
7. Polyak, K., Weinberg, R.A.: Transitions between epithelial and mesenchymal states: acquisition of malignant and stem cell traits. Nat. Rev. Cancer **9**(4), 265 (2009)
8. Karabacak, N.M., Spuhler, P.S., Fachin, F., Lim, E.J., Pai, V., Ozkumur, E., Martel, J.M., Kojic, N., Smith, K., Chen, P-i: Microfluidic, marker-free isolation of circulating tumor cells from blood samples. Nat. Protoc. **9**(3), 694 (2014)
9. Aghilinejad, A., Aghaamoo, M., Chen, X., Xu, J.: Effects of electrothermal vortices on insulator-based dielectrophoresis for circulating tumor cell separation. Electrophoresis **39**(5–6), 869–877 (2018). https://doi.org/10.1002/elps.201700264
10. Antfolk, M., Antfolk, C., Lilja, H., Laurell, T., Augustsson, P.: A single inlet two-stage acoustophoresis chip enabling tumor cell enrichment from white blood cells. Lab Chip **15**(9), 2102–2109 (2015)
11. Hou, H.W., Warkiani, M.E., Khoo, B.L., Li, Z.R., Soo, R.A., Tan, D.S.-W., Lim, W.-T., Han, J., Bhagat, A.A.S., Lim, C.T.: Isolation and retrieval of circulating tumor cells using centrifugal forces. Sci. Rep. **3**, 1259 (2013)
12. Huang, L.R., Cox, E.C., Austin, R.H., Sturm, J.C.: Continuous particle separation through deterministic lateral displacement. Science **304**(5673), 987–990 (2004)
13. Dincau, B.M., Aghilinejad, A., Hammersley, T., Chen, X., Kim, J.-H.: Deterministic lateral displacement (DLD) in the high Reynolds number regime: high-throughput and dynamic separation characteristics. Microfluid. Nanofluid. **22**(6), 59 (2018)
14. Lin, H.K., Zheng, S., Williams, A.J., Balic, M., Groshen, S., Scher, H.I., Fleisher, M., Stadler, W., Datar, R.H., Tai, Y.-C.: Portable filter-based microdevice for detection and characterization of circulating tumor cells. Clin. Cancer Res. **16**(20), 5011–5018 (2010)
15. Marrinucci, D., Bethel, K., Lazar, D., Fisher, J., Huynh, E., Clark, P., Bruce, R., Nieva, J., Kuhn, P.: Cytomorphology of circulating colorectal tumor cells: a small case series. J. Oncol. (2010). https://doi.org/10.1155/2010/861341
16. Meng, S., Tripathy, D., Frenkel, E.P., Shete, S., Naftalis, E.Z., Huth, J.F., Beitsch, P.D., Leitch, M., Hoover, S., Euhus, D.: Circulating tumor cells in patients with breast cancer dormancy. Clin. Cancer Res. **10**(24), 8152–8162 (2004)
17. McFaul, S.M., Lin, B.K., Ma, H.: Cell separation based on size and deformability using microfluidic funnel ratchets. Lab Chip **12**(13), 2369–2376 (2012)
18. Tan, S.J., Yobas, L., Lee, G.Y.H., Ong, C.N., Lim, C.T.: Microdevice for the isolation and enumeration of cancer cells from blood. Biomed. Microdev. **11**(4), 883–892 (2009)
19. Aghaamoo, M., Zhang, Z., Chen, X., Xu, J.: Deformability-based circulating tumor cell separation with conical-shaped microfilters: concept, optimization, and design criteria. Biomicrofluidics **9**(3), 034106 (2015)
20. Boey, S.K., Boal, D.H., Discher, D.E.: Simulations of the erythrocyte cytoskeleton at large deformation. I. Microscopic models. Biophys. J. **75**(3), 1573–1583 (1998)
21. Lim, C., Zhou, E., Quek, S.: Mechanical models for living cells—a review. J. Biomech. **39**(2), 195–216 (2006)
22. Leong, F.Y., Li, Q., Lim, C.T., Chiam, K.-H.: Modeling cell entry into a micro-channel. Biomech. Model. Mechanobiol. **10**(5), 755–766 (2011)
23. Evans, E., Yeung, A.: Apparent viscosity and cortical tension of blood granulocytes determined by micropipet aspiration. Biophys. J. **56**(1), 151–160 (1989)
24. Schmid-Schonbein, G., Shih, Y.Y., Chien, S.: Morphometry of human leukocytes. Blood **56**(5), 866–875 (1980)
25. Wandelt, B., Cywinski, P., Darling, G.D., Stranix, B.R.: Single cell measurement of micro-viscosity by ratio imaging of fluorescence of styrylpyridinium probe. Biosens. Bioelectron. **20**(9), 1728–1736 (2005)
26. Luby-Phelps, K., Taylor, D.L., Lanni, F.: Probing the structure of cytoplasm. J. Cell Biol. **102**(6), 2015–2022 (1986)
27. Zhou, E., Quek, S., Lim, C.: Power-law rheology analysis of cells undergoing micropipette aspiration. Biomech. Model. Mechanobiol. **9**(5), 563–572 (2010)
28. Tsai, M.A., Frank, R.S., Waugh, R.E.: Passive mechanical behavior of human neutrophils: power-law fluid. Biophys. J. **65**(5), 2078–2088 (1993)

29. Zhang, Z., Drapaca, C., Chen, X., Xu, J.: Droplet squeezing through a narrow constriction: minimum impulse and critical velocity. Phys. Fluids **29**(7), 072102 (2017)
30. Preetha, A., Huilgol, N., Banerjee, R.: Interfacial properties as biophysical markers of cervical cancer. Biomed. Pharmacother. **59**(9), 491–497 (2005)
31. Zhang, Z., Xu, J., Hong, B., Chen, X.: The effects of 3D channel geometry on CTC passing pressure-towards deformability-based cancer cell separation. Lab Chip **14**(14), 2576–2584 (2014)
32. Zhang, X., Chen, X., Tan, H.: On the thin-film-dominated passing pressure of cancer cell squeezing through a microfluidic CTC chip. Microfluid. Nanofluid. **21**(9), 146 (2017)
33. Zhang, Z., Chen, X., Xu, J.: Entry effects of droplet in a micro confinement: Implications for deformation-based circulating tumor cell microfiltration. Biomicrofluidics **9**(2), 024108 (2015)
34. Hodges, S., Jensen, O., Rallison, J.: The motion of a viscous drop through a cylindrical tube. J. Fluid Mech. **501**, 279–301 (2004)